Electrochemical Biosensor System Using A CMOS Microelectrode Array Provides High Spatially and Temporally Resolved Images

William Tedjo, Jasmine Nejad, Rachel Feeny, Lang Yang, Charles Henry, Tobet Stuart, Tom Chen

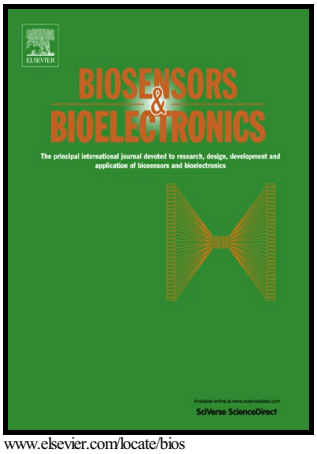

www.elsevier.com/locate/bios

PII: S0956-5663(18)30272-0
DOI: https://doi.org/10.1016/j.bios.2018.04.009
Reference: BIOS10405

To appear in: *Biosensors and Bioelectronic*

Received date: 30 December 2017
Revised date: 21 March 2018
Accepted date: 6 April 2018

Cite this article as: William Tedjo, Jasmine Nejad, Rachel Feeny, Lang Yang, Charles Henry, Tobet Stuart and Tom Chen, Electrochemical Biosensor System Using A CMOS Microelectrode Array Provides High Spatially and Temporally Resolved Images, *Biosensors and Bioelectronic,* https://doi.org/10.1016/j.bios.2018.04.009

Electrochemical Biosensor System Using A CMOS Microelectrode Array Provides High Spatially and Temporally Resolved Images

William Tedjo[a,1], Jasmine Nejad[b,1], Rachel Feeny[c], Lang Yang[a], Charles Henry[c], Tobet Stuart[b,d], Tom Chen[a,b,*]

[a] Department of Electrical & Computer Engineering, Colorado State University, Fort Collins, CO 80523, USA

[b] School of Biomedical Engineering, Colorado State University, Fort Collins, CO 80523, USA

[c] Department of Chemistry, Colorado State University, Fort Collins, CO 80523, USA

[d] Department of Biomedical Sciences, Colorado State University, Fort Collins, CO 80523, USA

***** Correspondence to: Tel: 970 491 6574. thomas.chen@colostate.edu

Abstract

The ability to view biological events in real time has contributed significantly to research in the life sciences. While video capture of real time changes in anatomical relationships is important, it is equally important to visualize real time changes in the chemical communications that drive cell behaviors. This paper describes an electrochemical imaging system capable of capturing changes in chemical gradients in live tissue slices. The system consists of a CMOS microchip with 8,192 configurable Pt surface electrodes, on-chip potentiostat, on-chip control logic, and a microfluidic device designed to interface with the CMOS chip to support *ex vivo* tissue experimentation. All data processing and visualization methods, sensor calibrations, microfluidics fabrication, and tissue preparation and handling procedures are described. Using norepinephrine as a target analyte for proof of concept, the system is capable of differentiating concentrations of norepinephrine as low as 8µM and up to 1,024 µM with a linear response and a spatial resolution of 25.5µm × 30.4µm. Electrochemical imaging was tested using murine adrenal tissue as a biological model and successfully showed caffeine-stimulated release of catecholamines from live slices of adrenal tissue with temporal sensitivity. This system successfully demonstrates the use of a high-density microelectrode array for electrochemical analysis with high spatiotemporal resolution to gather chemical gradient information in parallel with optical microscopy recordings.

Keywords

CMOS Biosensor; Microelectrode Array; Amperometry; Voltammetryl Electrochemistry; Ex Vivo Microfluidics; Data Visualization

1. Introduction

The ability to view biological events in real time contributes significantly to the understanding of critical life processes. Visualizing chemical changes at smaller dimensions and shorter timescales allows scientists to better understand the driving forces that regulate fundamental and obscure biological phenomena, such as chemotaxis and cancer metastasis. Traditional optical microscopy techniques provide a means of observing the movement of small molecules in live biological samples with spatial and temporal resolution, but have limitations. These methods are restricted to a library of inherently colored or fluorescent molecules and those

[1] Contributed equally to this work.

that can be selectively labeled through genetic modifications, exogenous fluorophores (Shashkova and Leake, 2017), or quantum dots (Wegner and Hildebrandt, 2015). In addition, these modifications add a considerable molecular weight when conjugated to small molecules such as neurotransmitters or pharmaceuticals, which can have a significant impact on behavior and function, making it difficult to visualize molecular changes in ways that replicate *in vivo* environments.

Electrochemical methods, such as scanning electrochemical microscopy (SECM) and microelectrode arrays (MEAs), have been previously explored as alternative methods for acquiring spatial and temporal chemical information from small molecules that cannot be reliably measured with existing microscopy techniques. SECM uses a microelectrode tip to scan the surface of a sample to measure the current generated by the reduction-oxidation (redox) of chemically active species, which can provide spatial chemical information, but is limited in its temporal resolution (Polcari et al., 2016). On the other hand, the MEA system approach provides a means of taking measurements from multiple electrodes simultaneously, allowing for improved spatial and temporal resolution (Forster, 1994; Obien et al., 2015). One of the first biological applications of MEAs utilized an array of thirty nickel-gold-platinum electrodes on a glass substrate to gather bioelectric measurements on the cellular level (Thomas et al., 1972). Over the years, the MEA system approach has substantially improved with the advancement of Complementary Metal-Oxide-Semiconductor (CMOS) manufacturing processes, which have allowed for the fabrication of higher density arrays capable of gathering spatially resolved electrical readings. Most of these CMOS-fabricated microchips have been used for bioelectric potential measurements and stimulation on electrogenic cells, such as neurons (Berdondini et al., 2009; Eversmann et al., 2003; Hierlemann et al., 2011) and cardiomyocytes (Heer et al., 2007). In addition, some CMOS-based MEA systems are capable of simultaneous electrochemical, impedimetric, potentiometric, and thermal measurements (Chi et al., 2015; Dragas et al., 2017; Niitsu et al., 2015). Our research introduces an electrochemistry-based imaging device based on redox reactions rather than bioelectric potential measurements which can be employed as a complementary platform within existing microscopy systems, allowing for simultaneous capturing of electrochemical and optical information.

The objective of this system is to demonstrate that redox-based electrochemical analytical techniques can be used to image biomarker release on live tissue samples using a high-density MEA, with proof of concept in the imaging of neurotransmitter release from live adrenal tissue upon stimulation with caffeine. Our device uses a three-electrode electrochemical cell with a working electrode (WE), reference electrode (RE), and auxiliary electrode (AE). The three-electrode system offers flexibility in performing various methods of electrochemical analysis, including amperometry, chronoamperometry, cyclic voltammetry, and differential pulse voltammetry. For this work, we chose to focus on amperometry, where the constant difference in potential between the WE and RE activates the reduction or oxidation of electrochemically-active compounds. Electron transfer from the redox reaction at the surface of the WE produces a current that is linearly proportional to the analyte concentration (Bard and Faulkner, 2000), enabling the determination of catecholamine concentration from current values. In prior work, our group demonstrated the effect of geometry on electrochemical response (Pettine et al., 2012) and established a method for interfacing MEA microchips

with microfluidics (Feeny et al., 2015; Wydallis et al., 2015). Preliminary live tissue electrochemical imaging results were reported along with a brief discussion of the system improvements (Tedjo et al., 2016). This manuscript provides a comprehensive discussion of the CMOS biosensor microchip design with hardware, software, and tissue handling protocols for gathering chemical readings from live tissue samples with high spatiotemporal resolution and demonstrates imaging of caffeine-stimulated catecholamine release from live murine tissue.

2. Materials and Methods

2.1 Biosensor Device Overview

The biosensor system is comprised of hardware, software, and methods for *ex vivo* electrochemical imaging. Fig. 1 describes the hardware and software integration, including the CMOS microchip, Printed Circuit Board (PCB), and data acquisition instrument as hardware components, and data processing methods with heatmap generation technique as software components. Section 2.2 to 2.5 discuss each of these components in detail.

Fig. 1. A simplified system level diagram of the high spatiotemporal resolution electrochemical imaging system.

2.2 Electrochemical Cell: Microelectrode Array Configuration

The CMOS biosensor microchip functions as a miniaturized electrochemical analysis device employing a three-electrode electrochemical cell system in an MEA configuration. Fabrication of the electrode array has been previously described (Wydallis et al., 2015). Each pair of WEs (Fig. 2A) has a spatial pitch of 25.5μm × 30.4μm to neighboring WE pairs. The interdigitated WE configuration is utilized to maximize current density flow while maintaining high spatial resolution (Bard, 2004; Pettine et al., 2012). Each subarray is a collection of 128 C-shaped electrodes, or 64 pairs of electrodes, enclosed by shared rectangular RE and AE (Fig. 2B). The entire array consists of 64 subarrays arranged in an 8 × 8 grid (Fig. 2C), which is equal to 8,192 individual C-shaped electrodes. All surface electrodes are raised 1.5μm above the microchip passivation surface and composed of metal layers of Ti, Au, and Pt, with Pt as the outermost layer to maintain electrical conductivity, mechanical stiffness, and biological compatibility.

At any given point in time, the 128 electrodes in a subarray can be selected and directly connected to the off-chip connection pins. The direct connection configuration allows simultaneous readings from all 128 electrodes in one subarray and can be cycled through different subarrays at a rate and spatial pattern determined by the user through the control logic. This direct connection architecture provides flexibility in modifying the configuration of the surface electrodes and in performing other methods of detection (e.g., impedimetric and potentiometric). The surface MEA configuration is visible as a 2.0mm × 2.0mm glossy square area in the middle of the silicon die (Fig. 2D).

Fig. 2. Hierarchy of biosensor hardware components. **(A)** Pair of WEs in a simplified interdigitated configuration. **(B)** A subarray consisting of a rectangular CE and RE on either side of the 128 individual (or 64

pairs of) WEs. **(C)** The entire 2.0mm × 2.0mm MEA with all 64 subarrays. **(D)** CMOS biosensor microchip die (19mm × 19mm) implanted in a 280-pin PGA ceramic package. **(E)** PCB platform electrochemical imaging with sockets for the switchable microchip, read channel array, low noise DC power regulator, and interface connection to the data acquisition board.

2.3 On-Chip: Potentiostat, Analog Switches, and Digital Logic Circuit

The potentiostat circuit was designed to facilitate various methods of electrochemical analysis, including amperometry, cyclic voltammetry, and differential pulse voltammetry. The on-chip potentiostat employs a simple single-ended Operational Amplifier (op-amp) unit. During the electrochemical reaction, the op-amp configuration forms a non-zero impedance path between the AE and the RE, setting the potential of the background environment to a desirable voltage. The op-amp circuit is based on a novel inverter-based topology (Figueiredo et al., 2010; Wilson et al., 2013) and its transistor level design and specifications were previously reported (Tedjo et al., 2016).

The analog switches, NMOS-PMOS transmission-gate (TG) switches, were responsible for switching groups of WEs between subarrays. The selected subarray is controlled by the user via 6-bit digital signals via the data acquisition board, which are connected to an on-chip 6-bit input to 64 outputs decoder, where one of 64 outputs from the decoder selects all 128 analog switches in the subarray being selected (Supplementary Information 1). This customized selection of subarrays allows the user to focus on a specific area of interest in the MEA. There is one analog TG switch for each of the 8,192 WEs in the MEA, however, the digital logic control only allows for one subarray to be simultaneously connected to the off-chip read-channels. The WE surface area was enlarged to increase electrochemical current input while maintaining the same electrical background noise. Each pair of the 128 WEs was externally shorted to make 64 larger WE pairs with increased electrode surface area. Fig. 2A shows two C-shaped electrodes that were shorted to form a single interdigitated WE.

The silicon-based microchip was custom designed and fabricated using 600nm CMOS technology with three metal layers for interconnects and the fourth metal layer for Pt-coated electrodes. As shown in Fig. 2D, the 19.0mm × 19.0mm CMOS microchip was packaged in a 280-pin ceramic pin grid array (IPKY8F, NTK Technologies). To prevent physical damage and unintentional electrical shorting during wet experiments, the wire-bonding area was sealed with a medical grade epoxy (EPO-TEK® 301, Epoxy Technology Inc.).

2.4 Circuit Board: Supporting Circuits & Read-Channels

The custom-designed FR-4 2-layer PCB board (330mm × 240mm), shown in Fig. 2E, houses the 280-pin socket, 64 read channels, power voltage regulators, bias voltage generator, and input-output headers. The 280-pin socket (Textool™ Burn-In Grid ZIP 200-6319-9UN-1900, 3M™) provides a platform for the switchable custom CMOS biosensor chip. Four low-dropout (LDO) voltage regulators (TPS7A33 and TPS7A4700, Texas Instrument) generate ultra-low noise dual-rail voltage, supplying ±1.5V to the MEA microchip and ±2.5V to the on-board read channels and all other components on the PCB. Two adjustable voltage generators deliver the necessary potential bias for the reference voltage of the on-chip potentiostat and the off-chip read channels.

Finally, 68-pin very-high-density cable interconnect (VHDCI) small computer system interface (SCSI) headers provide paths to the data acquisition board for 64 read channel outputs and 6-bit digital control input for subarray selection.

The read channels are constructed in the form of a current to voltage (I-V) converter. Fig. 3A depicts continuous trans-impedance amplifier (TIA) circuits converting electrical current inputs readings generated by 128 WE. Each read channel consists of a single-ended op-amp (OPA2376, Texas Instruments), a high precision 50MΩ ± 1% resistor (R_F), and a 1nF stabilization feedback capacitor (C_F). Details of read channel design and component selection for the op-amp, R_F, and C_F has been discussed previously (Tedjo et al., 2016).

2.5 Data Acquisition

The data acquisition is handled by a multichannel commercial data acquisition board with a custom-built MATLAB Graphical User Interface (GUI) with support from MATLAB Data Acquisition, Signal Processing, and Statistics Toolboxes (MATLAB, MathWorks). The data acquisition board (DAQ-2208, ADLINK Technology) provides up to 96-channel simultaneous sampling with a resolution of 12-bit analog to digital conversion. In order to sample all 64 read channels through time-multiplexing, the maximum sampling rate allowed by the DAQ-2208 architecture and MATLAB toolboxes is 240 data points per second per channel. The data acquisition board also supports up to 24 bits of digital input-output channels, six of which are being used to control the 6 to 64 decoder that regulates subarray selection. The 12-bit digitized data from the data acquisition board is fed in real time to the MATLAB GUI and simultaneously stored for offline data processing and conversion to a video of a heatmap. In addition to providing real-time acquisition for 64 channels, the MATLAB GUI (Supplementary Information 2) allows the user to manually configure subarray and read channel selection, subarray switching rate, sampling rate, and filtering options.

All tissue experiments used subarrays 1 through 64 with 0.5 second intervals between subarray switching and 240 samples per read channel per second. As data readings were gathered from the sensor, the output voltage from each read channel was displayed in real time and stored for offline processing. The stored data structure contained user input data (i.e., subarray and selected read channels), output voltage readings from each read channel, and time values for each output reading and each subarray switching event. The raw voltage data was post-processed in MATLAB for visualization.

2.6 Microfluidic System

The microfluidic system uses a multi-layer Y-shaped polydimethylsiloxane (PDMS) channel with two inlets and one outlet. The PDMS channel was developed to physically hold the tissue in place and to deliver stimulant while maintaining favorable conditions for live tissue during electrochemical imaging experiments. The main chamber of the PDMS channel, measuring 4mm wide, 6mm long, and 230µm tall, formed a sufficient space to confine a ~250µm thick, 3mm diameter tissue slice in the channel as portrayed in Fig. 3A. The main chamber consisted of two different layers. The bottom layer provided a space to hold the agarose-embedded tissue slice. The upper layer was designed to hold the 3mm diameter agarose-tissue slice down in contact with

the surface MEA while providing a ~230μm tall by 2mm wide channel for fluid to flow over the tissue. For limit of detection and dynamic range experiments, the Y-shaped microfluidic channel shown in Fig. 3 was modified to include an additional inlet hole between the existing two for cleaning purposes. Additionally, the geometry of the lower chamber was replicated for the upper chamber, creating a straight channel with a height of ~260μm for fluid flow without tissue.

Soft lithography and laser cutting techniques were used to create the channel features. As shown in Fig. 3B, a mold with multiple feature heights was created by assembling 230μm thick layers composed of pressure-sensitive adhesive (468MP-130μm, 3M™) and poly-film overhead transparency (PP2200-100μm, 3M™) on a clean polymethylmethacrylate (PMMA) plate. The PMMA base was cut to 25mm x 25mm and adhesive/transparency layers were laser cut to the desired geometries using a laser engraving system (Zing 16 Lasers, Epilog Laser). Fig. 3C shows the two layers of different compositions of PDMS used in the device. The bottom layer, directly in contact with the microchip, was ~460μm thick and made using PDMS (Sylgard 184, Dow Corning) at a 30:1 ratio of oligomer to cross-linker, creating a more adhesive layer to better seal the device and prevent leakage at the interface with the microchip. The top layer was ~4mm thick and comprised of a 10:1 ratio of oligomer to cross-linker, creating a more rigid polymer to maintain structural integrity and prevent excessive deformation of channel features. For each layer, the PDMS was degassed, poured into the mold, and cured for 30 minutes at 80°C. A 1mm biopsy punch was used to create inlet and outlet ports, which were connected to vinyl PVC tubing (1/32” ID, 3/32” OD, Thermo Fisher Scientific) using stainless steel connectors (Loctite, Henkel Corporation).

For all sensitivity characterization and tissue experiments, the outlet tubing was directed to a waste container and each inlet’s tubing was connected to a 10mL syringe (Benton, Dickinson and Company) driven by a syringe pump (NE-1000, New Era Pump Systems), allowing for control of flow rate for two types of fluids. To ensure flow stability, the PDMS device was held in place over the tissue with a custom-made compression plate laser cut from 0.125-inch thick PMMA. The plate contained holes matching the PDMS device to allow access to the inlet and outlet ports and holes for securing the plate to the microchip and imaging system board.

Fig. 3. Microfluidic setup and fabrication. **(A)** PMMA compression plate (top) and PDMS microfluidic device holding tissue down in contact with the electrochemical imaging microchip (bottom). **(B)** Layers of mold for rapid PDMS microfluidic prototyping. **(C)** Microfluidic device showing firmness and shape of each layer.

2.7 *Ex Vivo* Tissue Preparation

All animal experiments were carried out in accordance with the National Institutes of Health (NIH) Guide for the Care and Use of Laboratory Animals and the Institutional Animal Care and Use Committee Guidelines. An *ex vivo* organotypic slice model described previously (Tobet et al., 2003) was modified for use with adrenal tissue. In brief, male and female 8 to 12-week-old adult mice were deeply anesthetized with isoflurane and adrenal glands were removed following cervical dislocation. After removal, they were embedded in 8% agarose (39°C; Sigma, type VII-A), solidified at 4°C for four minutes, biopsy punched to 3mm, then sliced to 250μm thick in cold Krebs buffer (4°C; 126mM NaCl, 2.5mM KCl, 2.5mM CaCl2, 1.2mM NaH2PO4,

1.2mM MgCl2) using a vibrating microtome (VT1000S, Leica Biosystems). Slices were transferred to Hibernate-A medium (Gibco™) with 1% penicillin streptomycin (Hyclone Laboratories) in a polystyrene dish (Corning) on ice, incubated at 4°C for 15 minutes, then transferred to adult Neurobasal® medium (Gibco™) with 1.3% penicillin streptomycin, 5% B-27 Supplement (Gibco™), and 5% HEPES (Gibco™) at 37°C in a 5% CO2 incubator overnight prior to electrochemical imaging experiments. HEPES was added to maintain a stable physiological pH (7.1-7.4) during the recording process. The pH of media and solutions in the microfluidics and tissue preparation was tested throughout the experiment using standard litmus paper pH test strips.

2.8 *Ex Vivo* Electrochemical imaging

The system was enclosed in an environmental chamber with Olympus BX51/61QI microscope, as previously described (Tedjo et al., 2016), to imitate the internal conditions of the body by limiting light disturbances and maintaining a temperature of 37^{o}C. The microchip, imaging system board, and microfluidic device were placed under an optical microscope (BX61WI, Olympus) with a DSLR recording camera (D5500, Nikon), allowing for simultaneous optical and electrochemical imaging. Rubber-sealed access holes in the environmental chamber provided cable routes for connecting the power and signal sources to the imaging system board and for connecting the tubing from the inlet ports to the two syringe pumps outside of the chamber, allowing for instantaneous manual flow adjustments during the experiment.

Ex vivo experiments were carried out 24 hours after tissue collection, allowing the tissue to acclimate after stress induced by slicing. The tissue was then placed directly on the electrode array, after which the PDMS microfluidic device was positioned over the slice and secured with the compression plate setup. The inlet and outlet ports were connected to the microfluidic device and the syringe pump for media was immediately turned on to provide a constant flow of media over the tissue slice. All media used in the microfluidic system was Neurobasal® medium with 1.3% penicillin streptomycin, 5% B-27 Supplement, and 5% HEPES. Caffeine solutions used for stimulation were 55µM in media. Media and caffeine solutions were maintained at 37^{o}C at a pH of 7.1-7.4 and were administered at a flow rate of 20µL/min. The MATLAB GUI was used to gather baseline signal readings from the adrenal slice for three minutes under media flow, after which the media flow was switched to caffeine. Once caffeine reached the tissue slice, approximately two minutes after the switching point, signal recordings were taken for an additional 10 to 15 minutes. At the end of each experiment, the system was disassembled and the microfluidic system and microchip were flushed with DI-H_2O. For the amperometric detection of catecholamines, the class of neurotransmitters that includes epinephrine, norepinephrine, and dopamine, we used an oxidation potential of +0.6V (vs. Pt) (Wydallis et al., 2015). To measure the system performance in sensing neurotransmitters, media (Neurobasal®-A Medium, Gibco™) and a neurotransmitter ((±)-norepinephrine (+)-bitartrate salt, Sigma-Aldrich) solution dissolved in media were used as the blank sample and target analyte sample, respectively.

3. Results and Discussion

3.1 System Performance: Noise, Limit of Detection, and Dynamic Range

The limit of detection and dynamic range of the electrochemical sensor were quantified among different electrodes and read channels within the system to account for CMOS process variation. These data were measured by the relative signal change between the baseline signal of the culture media and the increased signal due to the presence of catecholamines.

The biosensor system delivered a significantly improved SNR than results previously reported (Wydallis et al., 2015). As shown in Fig. 4A, the low-noise LDO and enhanced read channels in the existing system generate about 100× less integrated noise ($I_{n\text{-}RMS}$ = 0.046nA$_{RMS}$) than previous system ($I_{n\text{-}RMS}$ = 3.611nA$_{RMS}$). The enhanced read channel design reduces overall flicker and white noise components, while the low-noise LDO suppresses the AC power line frequency component at 60Hz.

Each measurement was performed multiple times over a set of randomly selected electrodes, subarrays, and microchips. First, deionized water (DI-H_2O) was run through the center inlet, then switched to media flow through the first inlet, followed by media + norepinephrine flow through the second inlet. Once the signal of media + norepinephrine reached steady state, the value was recorded for three seconds, then the flow was switched back to blank medium and recorded for three seconds as the baseline. The side inlet flows were stopped and DI-H_2O was run through the center inlet to wash the surface electrode before continuing with another set of experiments. To conclude this process, the difference between the average three seconds recorded signals and baselines were calculated and recorded for each individual electrode and read channel. Using the data acquisition setup and MATLAB scripts, this procedure was automated and repeated multiple times with the same norepinephrine concentration to increase statistical accuracy and over a range of norepinephrine concentrations to generate the limit of detection and dynamic range data.

Fig. 4B shows the results from three microchips with randomly selected subarrays and electrodes in three separate experiments. In this series of sensitivity experiments, 512 samples were gathered for each concentration, resulting in a total of 4096 sample points for concentrations of 8µM, 32µM, 64µM, 128µM, 512µM, 1024µM, 2048µM, 4096µM. In general, the system showed a saturated response above 1024µM, a linear response from 8µM to 1024µM (defining the dynamic range), and a well-defined response at single digit µM concentrations. Since the data was collected based on the relative change from the baseline, the linear region (8µM to 1024µM) was fit to a regression equation without a zero intercept point, resulting in current (nA) equal to 3.35 times the concentration (mM), with a coefficient of determination, R^2 = 0.9913.

A further sensitivity investigation was performed and reported in Fig. 4C. The pre-calibration (red curves) and post-calibration (blue curves) results for blank media and 8µM to 128µM concentrations are presented in the form of a Probability Density Function (PDF). The calibration algorithm, as discussed in Section 3.2, effectively reduces variation and improves the distribution normality down to concentrations in the tens of µM. Mean (µ) and standard deviation (σ) values are listed and used to find limits of blank, detection, and quantitation, based on the CLSI-EP17-A Standard (Clinical and Laboratory Standards Institute, 2004). Table

Sensitivity of the biosensor system can be approximated by using of the device noise figure ($I_{n\text{-}RMS}$ = 0.046nA), the sensitivity curve at lower concentrations (8µM to 128µM), and the calculated Limit of Detection (LoD) value. The equivalent chemical concentration noise is $0.046nA_{RMS}$ /3.35 = $13.7\mu M_{RMS}$ and the LoD is 15.7µM. Therefore, the read channel maximum sensitivity can be approximated to be in the range between 10µM to 20µM. Even though the result was obtained using norepinephrine as a representative catecholamine, the limit of detection results for the biosensor system should be applicable to catecholamine in general. Table 1 summarizes and compared the significant properties to other published works in electrochemistry using MEA (Giagkoulovits et al., 2018; Levine et al., 2008; Nazari et al., 2013; Rothe et al., 2014).

Fig. 4. System performance summary. **(A)** Measured read channel noise spectrum shows improvement over previous system. **(B)** Electrochemical imaging system response and sensitivity curves with one-sigma distribution band. The reference line is a fitted linear line generated from 8µM to 1024µM concentrations. **(C)** Probability Density Function (PDF) of 8µM to 128µM concentration readings with corresponding Limit of Blank (LoB), Limit of Detection (LoD), and Limit of Quantitation (LoQ) values.

Table 1. Comparison of electrochemical biosensor system using CMOS MEA.

Parameter	Unit	(Levine et al., 2008)	(Nazari et al., 2013)	(Rothe et al., 2014)	(Giagkoulovits et al., 2018)	This Work
CMOS Technology	µm	0.25	0.35	0.35	0.35	0.6
Power Supply	V	2.5	3.3	3.3	3.3	3.3
Die Size	mm	5 × 3	3.8 × 3.1	7.5 × 4.8	3.79 × 3.79	19 × 19
Sensing Area	mm	N/A	3.15 × 1.9	3.2 × 3.2	1.81 × 1.81	2.2 × 2.2
WE Material	-	Au	Au	Pt Black	Au	Pt
WE Size	µm	70 × 70 to 100 × 100	100 (3D bumps)	Ø 5 - 50	20 × 20	17.5 × 15 (interdigitated)
WE Pitch	µm	N/A	200	100	114	25.5 x 30.4
Number of WEs	-	16	192	1024	256	8192
Number of Read Ch.	-	16	192	16	16	64
Bandwidth	kHz	10	1	0.1	150	10
Limit of Detection	nA	0.55	0.024	0.058	1.39	0.052
Power Dissipation	mW	N/A	36	N/A	125	120

3.2 Data Processing and Visualization

To extract accurate reads from the sensor, the output data was post-processed in MATLAB to remove subarray switching artifacts and minimize noise and interference. Figs. 5A and 5B show selected raw data recorded from subarrays 1 through 64 with 0.5 second intervals between subarray switching and 240 samples per read channel per second. As data readings were gathered from the sensor, the output showed spikes following each subarray switching event, after which the values settled to a steady point in a form similar to capacitor exponential decay. The form of these spikes is critical in the functionality of the electrochemical system, where a stable and continuous feedback loop incorporating the WE and AE is required to collect accurate read values.

Fig. 5A shows the unprocessed output of three selected read channels, out of 64. These channels represent the median, minimum, and maximum baseline values from the experiment, where the other channel readouts fall within this range. Most of the time-dependent drift is due to on-chip current leakage and electrode fouling of the MEA. Under a constant temperature, the typical baseline drift of the system was observed to be within 50pA/min. The experimental results in Fig. 5A were selected to show how the signal processing handles an extreme case of signal drift (2.8nA/min) over 270 seconds of *ex vivo* imaging.

During electrochemical imaging experiments, a rough estimation of the final heatmap can be made by observing patterns in the real-time voltage values displayed on the MATLAB GUI before any further data processing. The raw data shown in Fig. 5A correlates with the heatmap in Fig. 5C. The location of the tissue can be observed in the raw data as bumps, shown in subarrays 9 to 40, when compared to the flat regions seen in subarrays 1 to 8 and 41 to 64. In some cases, the magnitudes and trends of these bumps can also give a rough approximation of the pattern and shaped of the object being detected. To better visualize this data, a video of a heatmap was generated through the following offline data processing steps (further details in Supplemental Information 3):

1. Data Sampling – To accurately determine the sample at which the read channels switch to the next subarray, the locations of the voltage spikes were determined by finding the maximum values of the difference between each of the voltage signal readings, or taking the derivative of the data. The settled data values were then determined by taking the mean of the data while removing the outliers from a selected interval between peaks. The selected interval is 94% to 99% of the distance between peaks, portrayed as a thin shaded area before each peak in Fig. 5A. The resulting values are plotted in Fig. 5B.
2. Baseline Removal – The baseline was determined for each channel by taking the minimum values from each frame corresponding to regions of the array that were not under the tissue slice. These values were then fit using polynomial regression with a configurable order polynomial. The expected baseline values from the polynomial fit equations were then subtracted from the sample data, resulting in the baseline-corrected data shown in Fig. 5B. In this data, a 6th order polynomial provided sufficient baseline cancellation without adversely affecting the electrochemical signals.
3. Read Channel Calibration – This calibration minimizes gain variation between the 64 read channels due to feedback resistance variation, proximity of the WE to the CE (Pettine et al., 2012), and the variation in electrode interconnections as previously discussed in Section 2.2. Each calibration weight value was extracted from the scaled difference between read channel gain to the average of all channel gains. Finally, the weight value from each read channel was used to normalize output response, forcing the gain value closer to the gain average of all read channels.
4. Visualization – Minimum and maximum threshold values were set to remove extreme data values before mapping to MATLAB's 8-bit 'jet' color scale, represented by the numbers 0 (dark blue) to 255 (dark red). In this data, values below -0.3nA or above +2.0nA were translated to the lowest and highest values of the color map scale, 0 and 255, respectively. Fig. 5B provides the color-coded scatterplot for

each sampled signal. The color-scaled data values were then mapped to the electrode location within the corresponding subarray as shown in Fig. 5C.

5. Spatiotemporal Smoothing – To generate a continuous video over time, the data from each subarray was interpolated between each frame, creating a full frame of updated values for each new subarray reading to fill abrupt changes from one frame to the next. Outlying data values were removed and blended with the surrounding pixels through spatial averaging to prevent hotspots. The spatiotemporal smoothing algorithm improves heatmap visualization; although slightly altering the accuracy of the heatmap relative to the actual data.

The sources of noise and interference in the system include differences in read channel voltage gain, electrode surface morphology and size variation, and possible electrode biofouling. Various sources of inherent noise were removed using MATLAB in the post-processing calibration procedures. Variability in individual electrode readings due to slight differences in surface area or structure from the manufacturing process led to small amounts of variability between electrodes. These signal fluctuations were minimized in the final smoothing step in heatmap visualization.

Fig. 5. Data configuration and processing. **(A)** Raw data from three read channels representing the minimum (red), median (green), and maximum (blue) channel values. *Left:* raw data for the entire video, including voltage spikes. *Middle:* the first frame of the video. *Right:* Data from 4 subarrays, with the sampling regions (94-99% of each subarray) shown as a dot before each peak. (**B)** *Left:* the sampled (settled) data values over the entire video. *Middle:* data after baseline removal. *Right:* baselined data after thresholding, color-coded to the MATLAB jet scale shown on the right axis. (**C)** An example heatmap resulting from mapping the data to the actual physical location in the MEA.

3.3 Electrochemical Imaging of Live Tissue

In this experimental setup, we induce the release of primarily norepinephrine and epinephrine from the adrenal medulla, though small amounts of dopamine may also be present, as dopamine is a precursor for both of these molecules (Robinson et al., 2008). Since the catechol functional group that participates in the redox reaction is present in all three of these molecules and the applied potential of 0.6V is sufficient to activate oxidation of the hydroxyl groups, all three of these molecules are detected in our system. Though this system does not differentiate between these molecules, the total catecholamine concentration released from the tissue was calibrated from norepinephrine titrations representative of catecholamine oxidation. Detailed information about these redox reactions can be found in the Supplementary Information 4 (George J. Siegel, 2006; Pihel et al., 1994).

It is a well-understood limitation of amperometric detection of target analytes that it detects all electrochemically-active species in which the redox reaction can be activated at or below the applied potential. Therefore, knowledge of the species present in the system is important in amperometric detection and it will allow for more accurate determination of the molecule being detected. Specificity can be improved by using

cyclic voltammetry at each electrode, allowing for the detection of which electrochemically-active species are present in the sample and tailoring for specificity. However, the use of cyclic voltammetry for high-density MEAs will severely limit systems' temporal resolution.

Murine adrenal tissue offers an excellent biological model for demonstrating catecholamine release with spatial (e.g. gradients) and temporal components. Adrenal tissue has been well-studied (Martin et al., 2001; Petrovic et al., 2010; Xu et al., 2015) and releases high amounts of catecholamines (epinephrine, norepinephrine, and dopamine) in response to specific stimuli. The catecholamine release solely originates from the central medulla, without release from the surrounding cortex after stimulation with caffeine (Montgomery, 2012; Poisner, 1973; Spector et al., 1972). In this case, the electrochemical imaging device detected the amperometric current from catecholamine release without differentiating among epinephrine, norepinephrine, and dopamine.

Interfacing the tissue with the MEA required careful and rapid transfer of the tissue from the incubation petri dish to the electrode array using small spatulas, after which the PDMS microfluidic device was placed over the tissue and media flow injection was immediately initiated. Careful and swift tissue handling was critical in maintaining functional tissue and minimizing damage, as additional stress from excessive exposure to light, change in temperature and humidity, exposure to non-physiological oxygen conditions, lack of media, and physical pressure all had damaging effects on the tissue. In experiments with unscheduled prolonged handling times, tissue was discarded and other tissue slices were used to avoid bio-related reliability issues.

All experiments employed an identical microfluidic setup and comparable stimulant delivery timing that reached the MEA around five minutes after the beginning of signal acquisition. Live tissue electrochemical imaging yielded various chemical gradient results and patterns; however, they each depict a general trend showing localized release and clear correlation with the location of the tissue slice on the MEA. Fig. 6 illustrates time-lapsed screenshots of videos of three independent experiments (different murine adrenal glands) representing common results from *ex vivo* electrochemical imaging experiments employing the biosensor system. The results rely on relative measurement by calculating the signal of interest as the difference from the initial baseline, such that the heatmap indicates whether the readings are higher (more red) or lower (more blue) with respect to the baseline value calculated in Data Processing - Baseline Removal steps (Section 3.2).

The experimental results from tissue #1 were presented previously (Tedjo et al., 2016) and used as a reference to show the expected results from this type of electrochemical imaging experiment. Tissue #1 results show a well-defined chemical gradient pattern, enlargement, and localized increase in catecholamine concentration originating at the medulla towards the cortex after caffeine stimulation around t = 5min.

Tissue #2 results show common occurrences of inconsistent tissue activity (i.e., decreasing signal after caffeine stimulation) and electrochemical signal readings outside tissue area. First, the number of catecholamine-releasing chromaffin cells in this slice may have been low, resulting in spatially concentrated but brief catecholamine release patterns. Besides concerns in tissue quality, biofouling of the MEA could have also been a contributing factor in unreliable signal output. Biofouling is mostly caused by organic deposition,

hydrogen adsorption, and oxidation of the Pt electrode surface (French and Kuwana, 1964; Manica et al., 2003). Despite electrode treatments, biofouling still indicates some impairment of electron transfer functionality at the electrode and uneven readings from the MEA configuration. Second, non-electrochemically active areas, such as the adrenal cortex, create a high-impedance path that can disturb the baseline value calculation in a tissue experiment. In other words, the redox reactions occurring under the adrenal cortex area were dynamically lower than in flowing media surrounding the tissue slice. Tissue #2 results represent the population of experiments with complications in tissue quality, electrode biofouling, and electrode-tissue interfacing.

Tissue #3 results presented other challenges, with an initial spike of catecholamines concentrated in the medulla and accumulation of air bubbles. First, the high concentration readings at the beginning of the recorded phase correlated with when the biosensor device was initially turned on and the electrochemical reactions were initiated. The high current readings in the first frame (t = 0) suggest that the cells in the tissue released and accumulated a significant number of electrochemically active compounds at the surface of the MEA, resulting in rapid changes in electron flux once the recording was initially started. Moreover, excessive mechanical movement and stress induced during tissue placement on the MEA may have undesirably stimulated the chromaffin cells. Second, at t = 2 to 3 minute, air bubbles were observed entering between the MEA and tissue slice, where they resided for the rest of the experiment. These types of air bubbles may be trapped during the process of placing the tissue slice over the MEA or generated as a result of electrolysis at the MEA surface. Tissue #3 results represent the population of experiments with high initial readings and the presence of air bubbles.

Results from these experiments would not be sufficient to make biological inferences due to the challenges discussed above. Nevertheless, these results indicate there are well-defined spatial boundaries between the medulla, the cortex, and the area outside the tissue, demonstrating the potential of *ex vivo* high spatial resolution electrochemical imaging of tissue samples.

Fig. 6. Chemical heatmaps of *ex vivo* tissue experiments over three different murine adrenal tissue slices before and after caffeine stimulation. The scale bar, generated from the sensitivity curve, indicates catecholamine concentrations (up to 1.5 mM) specific to each experiment and tissue slice.

4. Conclusion

This paper presents a system-level solution for obtaining chemical images with high temporal and spatial resolution using a dense micro-electrode array. The system consists of custom-designed CMOS microchip with a Pt-coated MEA, supporting PCB with low noise read channels, and the supporting software with GUI for real-time monitoring capabilities. The integration of the key components in the system provides enhanced performance to allow for reliable sensing of micro-molar range catecholamine concentrations with 25.5μm × 30.4μm spatial resolution. In addition to demonstrating the capability of the high-resolution electrochemical imaging system, this study also provides necessary procedures for analysis of live tissue with

further considerations in sample preparation and handling for interfacing with the biosensor device with environmental control.

Future studies will aim to understand and address the current hardware, software, chemical, and biological integration challenges. Further considerations in the chemistry of the electrode-tissue interface are essential, such as the effects of diffusion in live three-dimensional tissue in the enclosed microfluidic system, as well as surface coatings and non-destructive cleaning protocols to minimize biofouling. Biological considerations of tissue viability, biocompatibility, and sustainable environmental control are also critical to increase the consistency and duration of experiments. In conclusion, the identification and minimization of all identifiable complications in the system is vital for accurate quantitative visualization of chemical gradients, which is becoming increasingly important in supporting and advancing biologically significant research.

Acknowledgements

The CMOS microchip, custom PCB, and the MATLAB GUI were initially developed and designed by Kristy Scholfield, Tucker Kern and, William Wilson from Electrical and Computer Engineering, Colorado State University (Fort Collins, CO). Biological tissue procedures were supported by Luke Schwerdtfeger and Chad Eitel from the Biomedical Sciences Department, Colorado State University (Fort Collins, CO). The CMOS microchip with platinum electrode array was manufactured by Broadcom Limited (Fort Collins, CO). This work was also partially supported by two grants from the National Science Foundation [GDE-0841259 and GDE-1450032].

References

Bard, A.J., 2004. Electrogenerated Chemiluminescence, Handbook of Electrochemistry: Pretreatment and Activation. Elsevier B.V. doi:10.1016/B978-0-444-51958-0.50026-4

Bard, A.J., Faulkner, L.R., 2000. Electrochemical Methods: Fundamentals and Applications, Electrochemistry. I. Faulkner, Larry R. doi:10.1016/B978-0-12-381373-2.00056-9

Berdondini, L., Imfeld, K., Maccione, A., Tedesco, M., Neukom, S., Koudelka-Hep, M., Martinoia, S., 2009. Active pixel sensor array for high spatio-temporal resolution electrophysiological recordings from single cell to large scale neuronal networks. Lab Chip 9, 2644. doi:10.1039/b907394a

Chi, T., Park, J.S., Butts, J.C., Hookway, T.A., Su, A., Zhu, C., Styczynski, M.P., McDevitt, T.C., Wang, H., 2015. A Multi-Modality CMOS Sensor Array for Cell-Based Assay and Drug Screening. IEEE Trans. Biomed. Circuits Syst. 9, 801–814. doi:10.1109/TBCAS.2015.2504984

Clinical and Laboratory Standards Institute, 2004. Protocols for Determination of Limits of Detection and Limits of Quantitation ; Approved Guideline.CLSI Document EP17-A, CLSI Document EP17-A.

Dragas, J., Viswam, V., Shadmani, A., Chen, Y., Bounik, R., Stettler, A., Radivojevic, M., Geissler, S., Obien, M.E.J., Muller, J., Hierlemann, A., 2017. In Vitro Multi-Functional Microelectrode Array Featuring 59760 Electrodes, 2048 Electrophysiology Channels, Stimulation, Impedance Measurement, and Neurotransmitter Detection Channels. IEEE J. Solid-State Circuits 52, 1–15.

doi:10.1109/JSSC.2017.2686580

Eversmann, B., Jenkner, M., Hofmann, F., Paulus, C., Brederlow, R., Holzapfl, B., Fromherz, P., Merz, M., Brenner, M., Schreiter, M., Gabl, R., Plehnert, K., Steinhauser, M., Eckstein, G., Schmitt-Landsiedel, D., Thewes, R., 2003. A 128 × 128 CMOS Biosensor Array for Extracellular Recording of Neural Activity. IEEE J. Solid-State Circuits 38, 2306–2317.

Feeny, R.M., Wydallis, J.B., Chen, T., Tobet, S., Reynolds, M.M., Henry, C.S., 2015. Analysis of Nitric Oxide from Chemical Donors Using CMOS Platinum Microelectrodes. Electroanalysis 27, 1104–1109. doi:10.1002/elan.201400510

Figueiredo, M., Santin, E., Goes, J., 2010. Biased CMOS Amplifier with High Efficiency. Analysis 2828–2831.

Forster, R.J., 1994. Microelectrodes: New Dimensions in Electrochemistry. Chem. Soc. Rev. 289–297. doi:10.1039/CS9942300289

French, W.G., Kuwana, T., 1964. Lifetime of Activated Platinum Surface. J. Phys. Chem. 68, 1279–1284. doi:10.1021/j100788a003

George J. Siegel, 2006. Basic Neurochemistry: Molecular, Cellular, and Medical Aspects, Journal of neurology, neurosurgery, and psychiatry. doi:10.1212/WNL.39.3.460-b

Giagkoulovits, C., Cheah, B.C., Al-Rawhani, M.A., Accarino, C., Busche, C., Grant, J.P., Cumming, D.R.S., 2018. A 16 x 16 CMOS Amperometric Microelectrode Array for Simultaneous Electrochemical Measurements. IEEE Trans. Circuits Syst. I Regul. Pap. 1, 1–11. doi:10.1109/TCSI.2018.2794502

Heer, F., Hafizovic, S., Ugniwenko, T., Frey, U., Franks, W., Perriard, E., Perriard, J.C., Blau, A., Ziegler, C., Hierlemann, A., 2007. Single-chip microelectronic system to interface with living cells. Biosens. Bioelectron. 22, 2546–2553. doi:10.1016/j.bios.2006.10.003

Hierlemann, B.A., Frey, U., Hafizovic, S., Heer, F., 2011. Growing Cells Atop Microelectronic Chips. Proc. IEEE 99.

Levine, P.M., Gong, P., Levicky, R., Shepard, K.L., 2008. Active CMOS sensor array for electrochemical biomolecular detection. IEEE J. Solid-State Circuits 43, 1859–1871. doi:10.1109/JSSC.2008.925407

Manica, D.P., Mitsumori, Y., Ewing, A.G., 2003. Characterization of electrode fouling and surface regeneration for a platinum electrode on an electrophoresis microchip. Anal. Chem. 75, 4572–4577. doi:10.1021/ac034235f

Martin, A.O., Mathieu, M.N., Chevillard, C., Guérineau, N.C., 2001. Gap junctions mediate electrical signaling and ensuing cytosolic Ca2+ increases between chromaffin cells in adrenal slices: A role in catecholamine release. J. Neurosci. 21, 5397–405.

Montgomery, D.C., 2012. Design and Analysis of Experiments, 8th ed. Wiley.

Nazari, M.H., Mazhab-Jafari, H., Leng, L., Guenther, A., Genov, R., 2013. CMOS neurotransmitter microarray: 96-channel integrated potentiostat with on-die microsensors. IEEE Trans. Biomed. Circuits Syst. 7, 338–348. doi:10.1109/TBCAS.2012.2203597

Niitsu, K., Ota, S., Gamo, K., Kondo, H., Hori, M., Nakazato, K., 2015. Development of Microelectrode Arrays Using Electroless Plating for CMOS-Based Direct Counting of Bacterial and HeLa Cells. IEEE Trans.

Biomed. Circuits Syst. 9, 607–619. doi:10.1109/TBCAS.2015.2479656

Obien, M.E.J., Deligkaris, K., Bullmann, T., Bakkum, D.J., Frey, U., 2015. Revealing neuronal function through microelectrode array recordings. Front. Neurosci. 9, 423. doi:10.3389/fnins.2014.00423

Petrovic, J., Walsh, P.L., Thornley, K.T., Miller, C.E., Wightman, R.M., 2010. Real-Time Monitoring of Chemical Transmission in Slices of the Murine Adrenal Gland 151, 1773–1783. doi:10.1210/en.2009-1324

Pettine, W., Jibson, M., Chen, T., Tobet, S., Nikkel, P., Henry, C.S., 2012. Characterization of novel microelectrode geometries for detection of neurotransmitters. IEEE Sens. J. 12, 1187–1192. doi:10.1109/JSEN.2011.2163708

Pihel, K., Schroeder, T.J., Wightman, R.M., 1994. Rapid and Selective Cyclic Voltammetric Measurements of Epinephrine and Norepinephrine as a Method To Measure Secretion from Single Bovine Adrenal Medullary Cells. Anal. Chem. 66, 4532–4537. doi:10.1021/ac00096a021

Poisner, A.M., 1973. Caffeine-Induced Catecholamine Secretion: Similarity to Caffeine-Induced Muscle Contraction. Proc. Soc. Exp. Biol. Med. 142, 103–105. doi:https://doi.org/10.3181/00379727-142-36967

Polcari, D., Dauphin-Ducharme, P., Mauzeroll, J., 2016. Scanning Electrochemical Microscopy: A Comprehensive Review of Experimental Parameters from 1989 to 2015. Chem. Rev. 116, 13234–13278. doi:10.1021/acs.chemrev.6b00067

Robinson, D.L., Hermans, A., Seipel, A.T., Wightman, R.M., 2008. Monitoring rapid chemical communication in the brain. Chem. Rev. 108, 2554–2584. doi:10.1021/cr068081q

Rothe, J., Frey, O., Stettler, A., Chen, Y., Hierlemann, A., 2014. Fully integrated CMOS microsystem for electrochemical measurements on 32 × 32 working electrodes at 90 frames per second. Anal. Chem. 86, 6425–6432. doi:10.1021/ac500862v

Shashkova, S., Leake, M.C., 2017. Single-molecule fluorescence microscopy review: shedding new light on old problems. Biosci. Rep. 0, BSR20170031. doi:10.1042/BSR20170031

Spector, S., Tarver, J., Berkowitz, B., 1972. Effects of Drugs and Physiological Factors in the Disposition of Catecholamines in Blood Vessels. Pharmacol. Rev. 24, 191 LP-202.

Tedjo, W., Feeny, R., Eitel, C., Schwerdtfeger, L., Willett, S., Henry, C., Tobet, S., Chen, T., 2016. Design of an integrated microelectrode array system for high spatiotemporal resolution chemical imaging, in: 2016 IEEE Biomedical Circuits and Systems Conference (BioCAS). IEEE, pp. 46–49. doi:10.1109/BioCAS.2016.7833721

Thomas, C.A., Springer, P.A., Loeb, G.E., Berwald-Netter, Y., Okun, L.M., 1972. A miniature microelectrode array to monitor the bioelectric activity of cultured cells. Exp. Cell Res. 74, 61–66. doi:https://doi.org/10.1016/0014-4827(72)90481-8

Tobet, S. a, Walker, H.J., Seney, M.L., Yu, K.W., 2003. Viewing cell movements in the developing neuroendocrine brain. Integr. Comp. Biol. 43, 794–801. doi:10.1093/icb/43.6.794

Wegner, K.D., Hildebrandt, N., 2015. Quantum dots: bright and versatile in vitro and in vivo fluorescence imaging biosensors. Chem. Soc. Rev. 44, 4792–4834. doi:10.1039/C4CS00532E

Wilson, W., Chen, T., Selby, R., 2013. A current-starved inverter-based differential amplifier design for ultra-

low power applications. 2013 IEEE 4th Lat. Am. Symp. Circuits Syst. LASCAS 2013 - Conf. Proc. doi:10.1109/LASCAS.2013.6519040

Wydallis, J.B., Feeny, R.M., Wilson, W., Kern, T., Chen, T., Tobet, S., Reynolds, M.M., Henry, C.S., 2015. Spatiotemporal norepinephrine mapping using a high-density CMOS microelectrode array. Lab Chip 15, 4075–4082. doi:10.1039/C5LC00778J

Xu, H., Zuo, P., Wang, S., Zhou, L., Sun, X., Hu, M., Liu, B., Wu, Q., Dou, H., Liu, B., Zhu, F., Teng, S., Zhang, X., Wang, L., Li, Q., Jin, M., Kang, X., Xiong, W., Wang, C., Zhou, Z., 2015. mouse model measured by electrochemical 3840–3845. doi:10.1039/c4an02074j

Highlights:

- A system level electrochemical biosensor with microelectrode array is discussed.
- Improvements and results of the hardware overall performance are presented.
- Data sets generated by the biosensor requires post-processing for visualization.
- Proper live tissue handling and preparation is crucial during the imaging process.
- Chemical image results of adrenal tissue ex vivo experiments are presented.